ORIGINAL ARTICLE

A 3D-printed scaffold with MoS$_2$ nanosheets for tumor therapy and tissue regeneration

Xiaocheng Wang[1,2,4], Tao Li[3,4], Hongshi Ma[1], Dong Zhai[1], Chuan Jiang[3], Jiang Chang[1], Jinwu Wang[3] and Chengtie Wu[1]

The treatment of malignant bone tumors is a significant clinical challenge because it requires the simultaneous removal of tumor tissues and regeneration of bone defects, and bifunctional three-dimensional (3D) scaffolds that function in both tumor therapy and tissue regeneration are expected to address this need. In this study, novel bifunctional scaffolds (MS-AKT scaffolds) were successfully fabricated by combining a 3D printing technique with a hydrothermal method. During the hydrothermal process, MoS$_2$ nanosheets were grown *in situ* on the strut surface of bioceramic scaffolds, endowing them with photothermal therapeutic potential. Under near-infrared (NIR) irradiation, the temperature of the MS-AKT scaffolds rapidly increased and was effectively modulated by varying the MoS$_2$ content, scaffold sizes and laser power densities. The photothermal temperature significantly decreased the viability of osteosarcoma cells and breast cancer cells and inhibited tumor growth *in vivo*. Moreover, the MS-AKT scaffolds supported the attachment, proliferation and osteogenic differentiation of bone mesenchymal stem cells and induced bone regeneration *in vivo*. This bifunctional scaffold, which treats the tumor and facilitates bone growth, offers a promising clinical strategy to treat tumor-induced bone defects. This proof-of-concept study demonstrates the feasibility of localized tumor therapy and tissue regeneration in diverse tissue engineering applications using multifunctional biomaterials.
NPG Asia Materials (2017) **9**, e376; doi:10.1038/am.2017.47; published online 21 April 2017

INTRODUCTION

In the clinic, malignant bone tumors are commonly treated using a combination of surgical resection, chemotherapy and radiotherapy.[1,2] However, surgical resection cannot completely eliminate tumor cells and simultaneously results in large bone defects that require repair using bioactive graft materials.[3,4] Moreover, chemotherapy and radiotherapy involve inevitable drawbacks, such as side effects on normal tissues and the tendency to induce drug resistance or radioresistance.[5,6] In recent years, photothermal therapy (PTT), a minimally invasive and highly efficient antitumor approach, has been demonstrated to enhance tumor therapeutic efficacy and reduce side effects in numerous pre-clinical animal studies.[2,7–10] PTT functions with the assistance of certain photothermal agents, which can convert near-infrared (NIR) laser light into heat and ablate tumor tissue by inducing hyperthermia.[2,11] Therefore, it is essential to fabricate a novel bifunctional biomaterial with photothermal therapeutic capacity for treating tumor cells and bone regeneration capacity for repairing bone defects derived from surgical resection.

Due to the high surface-area-to-mass ratio and unique optical properties, two-dimensional molybdenum disulfide (MoS$_2$) nanomaterials have recently been widely studied as an efficient photothermal agent for tumor ablation.[12–14] Chou *et al.*[13] first demonstrated that MoS$_2$ nanosheets exhibited ~ 7.8 times greater absorbance in the NIR region than graphene oxides, and their mass extinction coefficient ($\lambda = 800$ nm, $29.2 \, \text{lg}^{-1}$) was comparable to that of reduced graphene oxides ($24.6 \, \text{lg}^{-1} \, \text{cm}^{-1}$). In addition, previous studies have demonstrated that MoS$_2$ nanosheets possessed excellent photothermal therapeutic effects on tumors both *in vitro* and *in vivo*.[15–18] However, these studies primarily focused on simple tumor therapy using MoS$_2$ in the form of particles, which limits their application. Specifically, MoS$_2$ particles lack the desired mechanical strength and porous structure to induce bone regeneration after the surgical resection of tumor tissues and repair large tumor-induced bone defects. Bioactive materials used for tissue regeneration should be highly porous to induce cell migration, nutrient transportation and tissue ingrowth.[19–22] Thus, we hypothesized that a porous MoS$_2$ scaffold may be able to treat large tumor-induced bone defects by

[1]State Key Laboratory of High Performance Ceramics and Superfine Microstructure, Shanghai Institute of Ceramics, Chinese Academy of Sciences, Shanghai, People's Republic of China; [2]University of Chinese Academy of Sciences, Beijing, People's Republic of China and [3]Shanghai Key Laboratory of Orthopaedic Implant, Department of Orthopaedic Surgery, Shanghai Ninth People's Hospital Affiliated Shanghai Jiao Tong University School of Medicine, Shanghai, People's Republic of China
[4]These authors contributed equally to this work.
Correspondence: Professor C Wu or Professor J Chang, State Key Laboratory of High Performance Ceramics and Superfine Microstructure, Shanghai Institute of Ceramics, Chinese Academy of Sciences, 1295 Dingxi Road, Shanghai 200050, People's Republic of China.
E-mail: chengtiewu@mail.sic.ac.cn or jchang@mail.sic.ac.cn
or Professor J Wang, Shanghai Key Laboratory of Orthopaedic Implant, Department of Orthopaedic Surgery, Shanghai Ninth People's Hospital Affiliated Shanghai Jiao Tong University School of Medicine, 639 Zhizaoju Road, Shanghai 200011, People's Republic of China.
E-mail: wangjw@sjtu.edu.cn
Received 28 August 2016; revised 21 November 2016; accepted 4 February 2017

2

harnessing its inherent photothermal properties and the osteogenic potential of porous scaffolds.

Three-dimensional (3D)-printed bioceramic scaffolds have been widely used for bone regeneration in recent decades because their precise interconnected macropore-structure benefits nutrient transportation and cell ingrowth and their bioactive elements can induce osteogenesis and angiogenesis.[19,20] When implanted into bone defects in vivo, they can induce new bone ingrowth to rapidly promote osteo-integration and bone remodeling. Moreover, these scaffolds gradually degrade as new bone tissue is formed. Thus, such a bioactive 3D scaffold containing MoS$_2$ is expected to exhibit both the mechanical strength and porous structure for repairing tumor-induced bone defects. Notably, molybdenum (Mo) is an essential trace element for animals and humans that serves as a cofactor for sulfite oxidase (SO) and xanthine oxidase (XO).[23] Early animal experiments in chicks, poults, mice and pigs showed that Mo can stimulate early development in a dose-dependent manner.[23–26] Moreover, Mo-containing metals and alloys (for example, Ti-7.5Mo,[27] Ti-15Mo-1Bi,[28] Co-Cr-Mo[29] and Ti-12Mo-6Zr-2Fe[30]) exhibited excellent mechanical properties and biocompatibility and have been widely used as orthopedic and dental implants. However, to the best of our knowledge, studies of Mo-containing tissue engineering scaffolds for bone regeneration have not yet been reported. Therefore, the surface modification of 3D-printed bioceramic scaffolds using MoS$_2$ nanosheets is hypothesized to combine the bone-forming ability of silicate bioceramic scaffolds with PTT for treating large tumor-induced bone defects.

Herein, a bifunctional scaffold was prepared by growing MoS$_2$ nanosheets on 3D-printed bioceramic scaffolds in situ via combining a 3D printing technique with a hydrothermal method. Akermanite (AKT, Ca$_2$MgSi$_2$O$_7$), a Ca-, Mg- and Si-containing bioceramic, was selected as the matrix material for carrying MoS$_2$ nanosheets because it readily promotes osteogenesis and angiogenesis, as shown in our previous study.[31,32] The structure and composition of the MoS$_2$-modified AKT (MS-AKT) scaffolds were characterized by optical microscopy, scanning electron microscopy (SEM), X-ray diffraction (XRD) and X-ray photoelectron spectroscopy (XPS). The photothermal performance of the scaffolds was then systematically investigated by altering the scaffold sizes, laser power densities and MoS$_2$ content. Furthermore, the photothermal therapeutic capacity of MS-AKT scaffolds was evaluated by measuring the viability of tumor cells in vitro and ablating tumor tissue in vivo. Finally, the biocompatibility and bone-forming ability of MS-AKT scaffolds were investigated by culturing rabbit bone mesenchymal stem cells (rBMSCs) in vitro and repairing bone defects in vivo.

EXPERIMENTAL PROCEDURES
Preparation of MS-AKT scaffolds
AKT bioceramic scaffolds with uniform macroporous morphologies were prepared using a 3D printing technique. In brief, 5 g of AKT powder (Kunshan Chinese Technology New Materials Co., Ltd., Kunshan, China), 0.32 g of alginic acid sodium salt (Alfa Aesar, Shanghai, China) and 2.5 g of Pluronic F127 solution (Sigma-Aldrich, 20 wt.% in H$_2$O) were stirred until homogeneous, loaded into a printing tube and then printed via a printing needle (20 G) to obtain the raw AKT scaffolds. The raw scaffolds were then dried at room temperature and sintered at 1350 °C for 3 h to obtain AKT scaffolds.

A facile hydrothermal method was applied to fabricate MS-AKT scaffolds. In brief, to prepare 0.2 MS-AKT scaffolds, 1 mmol of ammonium molybdate ((NH$_4$)$_6$Mo$_7$O$_{24}$·4H$_2$O) and 30 mmol of thiourea (H$_2$NCSNH$_2$) were dissolved in 35 ml of distilled water under vigorous stirring to form a homogeneous solution ([Mo] = 0.2 mol l^{-1}). The solution was transferred into a 100 ml Teflon-lined stainless steel autoclave containing 4 g of AKT scaffolds.

The reaction system was maintained at 180 °C for 24 h. The black scaffolds were collected, washed and dried at 60 °C under vacuum. 0.1 MS-AKT and 0.05 MS-AKT scaffolds were similarly prepared using different concentrations of (NH$_4$)$_6$Mo$_7$O$_{24}$·4H$_2$O and thiourea ([Mo] = 0.1, 0.05 mol l^{-1}). Pure MoS$_2$ particles were similarly prepared at 180 °C without AKT scaffolds, as previously reported.[33]

Characterization of scaffolds
The overall microscopic images of MS-AKT and AKT scaffolds were obtained using an optical microscope (S6D, Leica, Germany). The morphology and elemental mapping of the scaffolds were examined with a scanning electron microscope (SEM, S-4800, Hitachi, Tokyo, Japan) equipped with an energy-dispersive spectrometer. The crystal structure and phases of the samples were characterized by XRD (D8 ADVANCE, BRUKER AXS GMBH, Karlsruhe, Germany). XPS measurements were performed on a special spectrometer (XPS, ESCAlab250, Thermo Fisher Scientific, Waltham, MA, USA). The concentrations of Mo, Ca, Mg and Si were measured by inductively coupled plasma-atomic emission spectrometry (ICP-AES, Vista AX, Varian, Palo Alto, CA, USA).

Photothermal effects of MS-AKT scaffolds
The photothermal effects of the MS-AKT scaffolds were investigated in a 48-well culture plate under dry (air) and wet (500 μl phosphatic buffer solution (PBS)) conditions. An 808-nm laser beam (diameter: 12 mm) was focused on the scaffolds (Φ8.5 mm × 3 mm) for 5 or 10 min. The light-induced temperature changes and thermal images of scaffolds of different sizes (diameter: 6, 8.5 and 11 mm), laser power densities (0.2, 0.3, 0.4, 0.5 and 0.6 W cm^{-2}) and MoS$_2$ concentrations (0.2, 0.1 and 0.05 M) were monitored in real time and recorded by an infrared thermal imaging system (PM100D, Thorlabs GmbH, Munich, Germany).

In vitro anticancer effects of MS-AKT scaffolds
Two tumor cell lines, Saos-2 cells (osteosarcoma cells) and MDA-MB-231 cells (breast cancer cells, the most commonly used bone metastatic tumor cell line), were cultured in minimum essential medium alpha medium (Gibco) containing 10% fetal bovine serum (FBS, HyClone) in a humidified incubator (5% CO$_2$ at 37 °C). To test cell viability, the cells were cultured on 24-well plates for 24 h (2.0 × 10^4 per well, 1 ml medium), and the 0.2 MS-AKT and AKT scaffolds (Φ11 mm × 3 mm) were then gently placed onto the plates. Tumor cells grown with 0.2 MS-AKT scaffolds, AKT scaffolds or without scaffolds were irradiated with an NIR laser (0.6 W cm^{-2}, 10 min). As a control, cells were cultured with scaffolds under the same conditions without irradiation. After 24 h, the cell viability was quantified with a CCK8 assay. First, the culture medium and scaffolds were removed, and 20 μl of CCK8 solution and 180 μl of medium were then added to each well. After 1.5 h, 100 μl of the solution was aspirated from each well and added to a fresh 96-well plate. Subsequently, the absorbance was measured at 450 nm using a microplate reader (Epoch, BIO-TEK, Winooski, VT, USA).

To evaluate the effect of irradiation duration on cell viability, the Saos-2 cells and 0.2 MS-AKT scaffolds were irradiated with an NIR laser (0.6 W cm^{-2}, one time) for 5, 10, 15 and 20 min. The tumor cell viability was measured with a CCK8 assay as described above. To evaluate the effect of irradiation time on the cell viability, the Saos-2 cells were cultured with MS-AKT scaffolds as described above and irradiated with an NIR laser (0.6 W cm^{-2}, 10 min). After 12 h, the viability of the four samples was measured with a CCK8 assay, and the remaining four samples were again irradiated with an NIR laser before being subjected to a CCK8 assay 12 h later. The process was repeated once again. To evaluate the effect of different power densities (temperature) on the cell viability, an infrared thermal camera was used to observe temperature variations. Each sample was irradiated for 10 min, and the tumor cell viability was also measured with a CCK8 assay, as described above.

Saos-2 cells were cultured in MS-AKT or AKT scaffolds (Φ11 mm × 3 mm) on 48-well plates (1.0 × 10^4 cells per well, 500 μl of medium) and irradiated (0.6 W cm^{-2}, 10 min, one time). Control cells were not irradiated. After 12 h, the cells were post-fixed with 2.5% glutaraldehyde, followed by a graded ethanol series (30, 50, 70, 90, 80, 95 and 100 v/v%) before being dried in

hexamethyldisilazane. The morphology of Saos-2 cells on MS-AKT and AKT scaffolds was observed by SEM (SU8220, Hitachi).

To qualitatively evaluate the photothermal effect of MS-AKT scaffolds on the surrounding tumor cells, Saos-2 cells and MDA-MB-231 cells were seeded in 24-well culture plates containing glass slides and incubated at 37 °C for 24 h. MS-AKT and AKT scaffolds were placed onto the glass slides and irradiated (0.6 W cm^{-2}, 10 min, one time). The scaffolds were then removed, and any cells on the glass slides were stained with Ethidium homodimer-1 and Calcein AM. The remaining four samples were incubated for another 12 h, and the cytoskeleton and nuclei were stained with rhodamine phalloidin and DAPI (Cytoskeleton Inc., Denver, CO, USA). The cellular samples were observed using fluorescence confocal microscopy (Leica TCS SP8).

### *In vivo* tumor therapy of MS-AKT scaffolds

The tumor-bearing mouse model was constructed as described in our previous study.[3] Saos-2 tumor cells (5×10^6 cells) were subcutaneously injected into the backs of Balb/c mouse (4–6 weeks old). When the tumor reached ~ 10 mm in diameter, the mice were randomly divided into four groups ($n = 5$): (i) MS-AKT+Laser group; (ii) MS-AKT group; (iii) AKT+laser group; and (iv) AKT group. A skin incision was made at the edge of the tumor, and the scaffolds (0.2 MS-AKT or AKT scaffolds, 8 mm × 2 mm × 2 mm, Supplementary Figure S12a) were then implanted into the center of the tumors. For the laser treatment groups, each mouse was exposed to the NIR laser (0.5 W cm^{-2}, 10 min), and the tumor surface temperature was recorded (Supplementary Figure S13). The first NIR treatment was defined as day 0. Starting on day 0, the length and width of the tumor were measured with calipers before irradiation treatment every 2 days. The tumor sizes were calculated as follows: tumor volume (V) = (tumor length) × (tumor width)^2/2 − scaffold volume. The relative tumor volumes (V_r) were calculated as follows: $V_r = V/V_0$ (V_0 = tumor volume on day 0–scaffold volume). Whole-body bioluminescent imaging was performed on days 0 and 7. The mice were killed on day 14, and the treated tumors were harvested and fixed in 4% neutral buffered formalin, embedded in paraffin, sectioned and stained with hematoxylin and eosin (H&E) before being evaluated under a light microscope (Leica, DM4000B). Five sections were selected from each sample, and five fields were randomly examined for each section. In addition, five sections from normal tumors without NIR treatment and scaffold implantation were simultaneously stained. The tumor cell necrosis rate was calculated as follows: tumor cell necrosis rate = $(1 - N/M) \times 100\%$. Here, N is the mean number of surviving tumor cells in scaffolds, and M is the mean number of surviving tumor cells in normal, untreated tumor tissue sections.

In vitro attachment, proliferation and osteogenic differentiation of rBMSCs

rBMSCs (bone-forming cells) and specialized medium were purchased from Cyagen Biosciences. In brief, 5.0×10^3 rBMSCs (four passages) were seeded in 48-well culture plates. After 24 h, a 0.05 MS-AKT or AKT scaffold ($\Phi 8.5$ mm × 3 mm, $n = 5$) was transferred into the above culture plates, and the cells were incubated for 1, 3 and 7 days. Cell proliferation was measured with a CCK8 assay as described above.

Moreover, 1.0×10^4 rBMSCs were seeded in scaffolds placed in 48-well culture plates and incubated for 3 days. The medium was removed, and the scaffolds were fixed with glutaraldehyde and then dehydrated in a graded ethanol series and hexamethyldisilazane. The morphological characteristics of rBMSCs on MS-AKT and AKT scaffolds were observed by s.e.m.

To further investigate the effect of ionic products released from MS-AKT scaffolds on cell proliferation, ionic extracts were prepared from scaffolds by adding 0.2 MS-AKT or AKT scaffolds to basal culture medium according to the procedures reported in the literature[34] at a ratio of scaffold to medium of 200 mg ml^{-1}. After incubation at 37 °C for 24 h, the supernatant was collected and filtered through a 0.22 μm filter. The resulting supernatant was supplemented with 10% FBS, 1% penicillin-streptomycin and 1% L-Glutamine and denoted the original extract. Serial dilutions of extracts were prepared by diluting the original extract x times ($x = 2, 4, 8, 16, 32$ or 64) with complete medium to obtain the final extracts (denoted as $1/x$ extracts). The proliferation of rBMSCs was measured with a CCK8 assay. In brief, 1×10^3 rBMSCs were
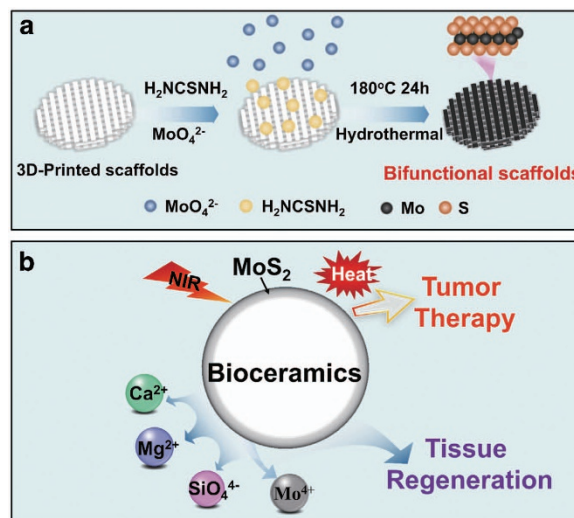
Scheme 1 Schematic illustrations of the *in situ* growth of MoS$_2$ nanosheets on 3D-printed bioceramic scaffolds (**a**) and their bifunctions of tumor therapy and tissue regeneration (**b**). During the hydrothermal process, MoS$_2$ nanosheets were *in situ* grown on the strut surface of bioceramic scaffolds, forming a core/shell structure with a bioceramic core and MoS$_2$ shell. The MoS$_2$ layer endows the scaffolds with photothermal therapeutic capacity, and meanwhile the soluble Ca, Si, Mg and Mo ions released from the scaffolds can stimulate tissue regeneration.

seeded in 96-well culture plates ($n = 6$). After 24 h, the culture medium was removed and replaced with 100 μl of serially diluted extracts. After 1, 3 and 7 days, the old medium was replaced with 10 μl of CCK8 solution and 90 μl of cell culture medium. After incubation for 1.5 h, the absorbance was measured at 450 nm using a microplate reader.

The expression of bone-related genes by rBMSCs in the MS-AKT and AKT scaffolds, as well as their extracts, was evaluated by real-time PCR. Specifically, the messenger RNA expression levels of OPN, OCN, Runx2 and ALP were measured. To this end, the rBMSCs were seeded in scaffolds and cultured for 7 days, and TRIzol Reagent was used to isolate the total RNA. The relative gene expression levels were obtained after normalization against the Ct value of the housekeeping gene.

In vivo bone regeneration under short-term photothermal treatment

All rabbits were treated in accordance with the guidelines of the Animal Care and Use Committee of the Ninth People's Hospital of Shanghai Jiao Tong University. Six New Zealand white male rabbits (2.5–3 kg) were selected to evaluate bone regeneration by MS-AKT and AKT scaffolds using the standard femoral defect model. Two critical-sized defects ($\Phi 8$ mm × 5 mm) were created in the interior of the distal femoral condyle of the left and right posterior limbs. The 0.2 MS-AKT and AKT scaffolds ($\Phi 8$ mm × 5 mm, Supplementary Figure S12b) were implanted into the right and left femoral defects, respectively. Here, we established large bone defect models in rabbits instead of nude mice as used in the tumor therapy assay because establishing critical-sized bone defects in mice is difficult and unconvincing considering the small size of mouse bones and the large size of the scaffolds. To explore the effects of short-term PTT on long-term bone regeneration, the scaffolds were exposed to NIR irradiation (0.5 W cm^{-2}, 10 min, Supplementary Figure S14a), and the incisions were closed in layers after irradiation. The rabbits were killed after 8 weeks, and the femoral-scaffold complex samples were immediately collected for micro-computerized tomography (CT) analysis. All the bone tunnel model images were acquired with a Micro-CT scanner (μCT100, SCANCO Medical, Zurich, Switzerland), and the relative bone volume fractions (BV/TV) in defect regions were measured. Histological analyses were carried out using Van Gieson's picrofuchsin stain, and the tissues were examined under a light microscope (Leica, DM4000B).
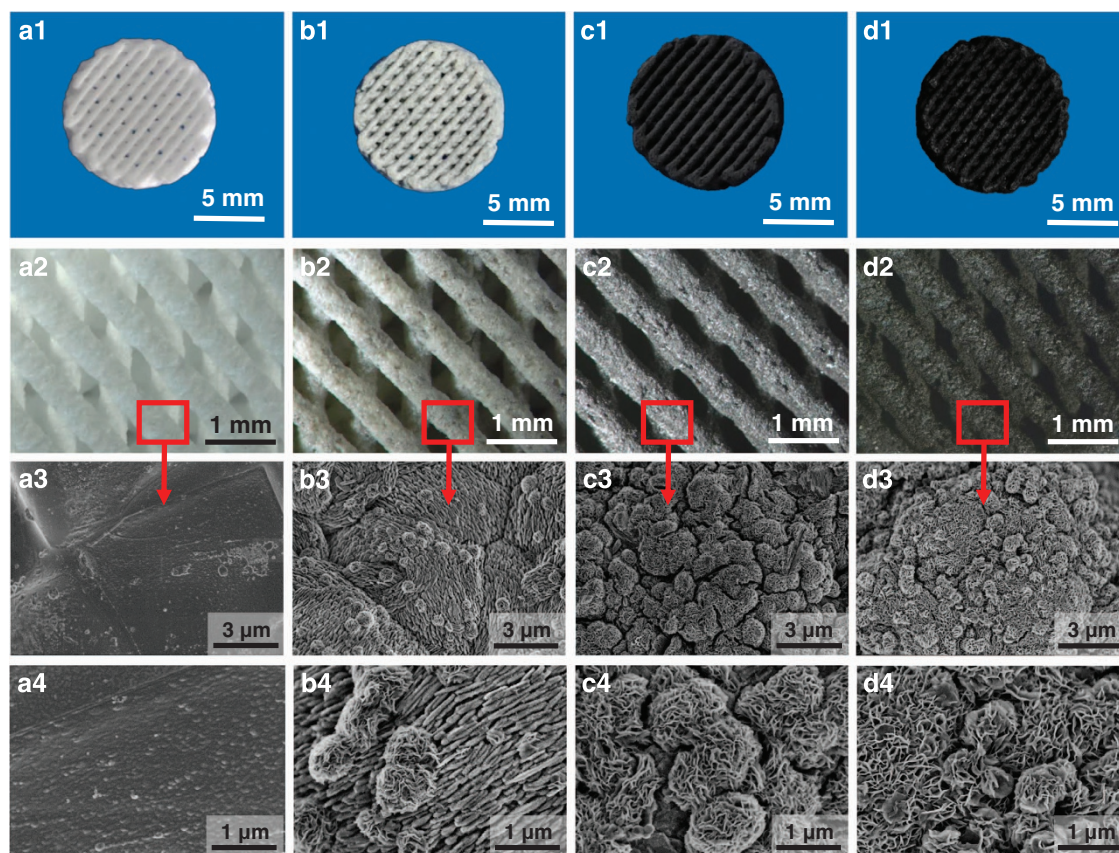
4

Figure 1 Photograph of 3D-printed akermanite (AKT) (a$_1$), 0.05 MoS$_2$-modified akermanite (MS-AKT) (b$_1$), 0.1 MS-AKT (c$_1$) and 0.2 MS-AKT (d$_1$) scaffolds; optical images of AKT (a$_2$), 0.05 MoS$_2$-modified akermanite (MS-AKT) (b$_2$), 0.1 MS-AKT (c$_2$) and 0.2 MS-AKT (d$_2$) scaffolds. Scanning electron microscope (SEM) images on the pore wall of AKT (a$_3$ and a$_4$), 0.05 MS-AKT (b$_3$ and b$_4$), 0.1 MS-AKT (c$_3$ and c$_4$) and 0.2 MS-AKT (d$_3$ and d$_4$) scaffolds. The AKT scaffolds with well-designed morphology appeared white, while the color of MS-AKT changed from light to dark black and there were more MoS$_2$ nanosheets or nanoflowers growing on the strut surface of AKT scaffolds with the increase of the concentrations of Mo and S sources in the hydrothermal reaction solutions.

Statistical analysis

All data are expressed as the means ± s.d. and were analyzed using a one-way analysis of variance statistical analysis to evaluate the significance of differences. A *P*-value < 0.05 was considered to indicate significant differences, which are denoted by the following: $*P<0.05$, $**P<0.01$ and $***P<0.001$.

RESULTS

Preparation and characterization of MS-AKT scaffolds

In this study, a novel bifunctional scaffold was successfully prepared by combining a 3D printing technique with a hydrothermal method (Scheme 1a). The AKT scaffolds exhibited well-designed morphology and appeared white (Figure 1a$_1$ and a$_2$), whereas MS-AKT scaffolds changed from a light color to dark black (Figure 1b$_1$,b$_2$,c$_1$,c$_2$,d$_1$ and d$_2$) as the concentrations of Mo and S resources in the hydrothermal reaction solution increased. SEM images showed that AKT scaffolds possessed a dense and smooth surface without nanostructures (Figure 1a$_3$ and a$_4$ and Supplementary Figure S2a). However, after the hydrothermal treatment, a newly generated layer of ultrathin MoS$_2$ nanosheets uniformly covered the entire strut surface of the AKT scaffolds (Figure 1b$_3$–d$_3$ and b$_4$–d$_4$ and Supplementary Figure S2b and c) and the thickness of MoS$_2$ nanosheets directly correlated with the Mo and S concentrations. The morphology of the MoS$_2$ layer on the scaffold surface was similar to that of pure MoS$_2$ particles prepared via the hydrothermal route (Supplementary Figure S1). Interestingly,

the MS-AKT scaffold exhibited a marked core/shell structure that consisted of an AKT core and an ~5-µm-thick MoS$_2$ shell (Figure 2a–c), and this layered structure was well retained after ultrasonication for 1 h (Supplementary Figure S3). The elemental components of the MS-AKT scaffold cross-section were examined by energy-dispersive spectrometer mapping analysis, which showed that the Mo and S signals tended to increase, whereas the Ca, Mg, Si and O signals tended to decrease from the interior to the strut surface (Figure 2d–f and Supplementary Figure S4). The line scanning profiles of all elements displayed a step profile from the interior to the strut surface of the scaffolds (Figure 2g–i and Supplementary Figure S5). The characteristic peaks of Mo, S, Ca, Mg, Si and O could be readily detected on the strut surface of the MS-AKT scaffolds using XPS (Figure 3b), and the atomic percentages of Mo and S were 8.6 and 17.9%, respectively. As shown in Figure 3c and d, the peaks for Mo 3d (232.1, 228.8 eV) and S 2p (162.8, 161.7 eV) of MoS$_2$ nanosheets on scaffolds slightly shifted to lower binding energies compared to that of pure MoS$_2$ particles (Mo 3d: 232.2, 229.0 eV; S 2p: 163.0, 161.9 eV). These results provided direct evidence to show that the nanosheets on AKT scaffolds consisted of MoS$_2$, with a Mo valence state of +4 and an S valence state of − 2. The XRD analysis of MoS$_2$ particles, MS-AKT and AKT scaffolds (Figure 3a) showed that the diffraction peaks of AKT scaffolds matched the standard pattern of the AKT crystal phase (JCPDS card no. 35–0592), and five broadened
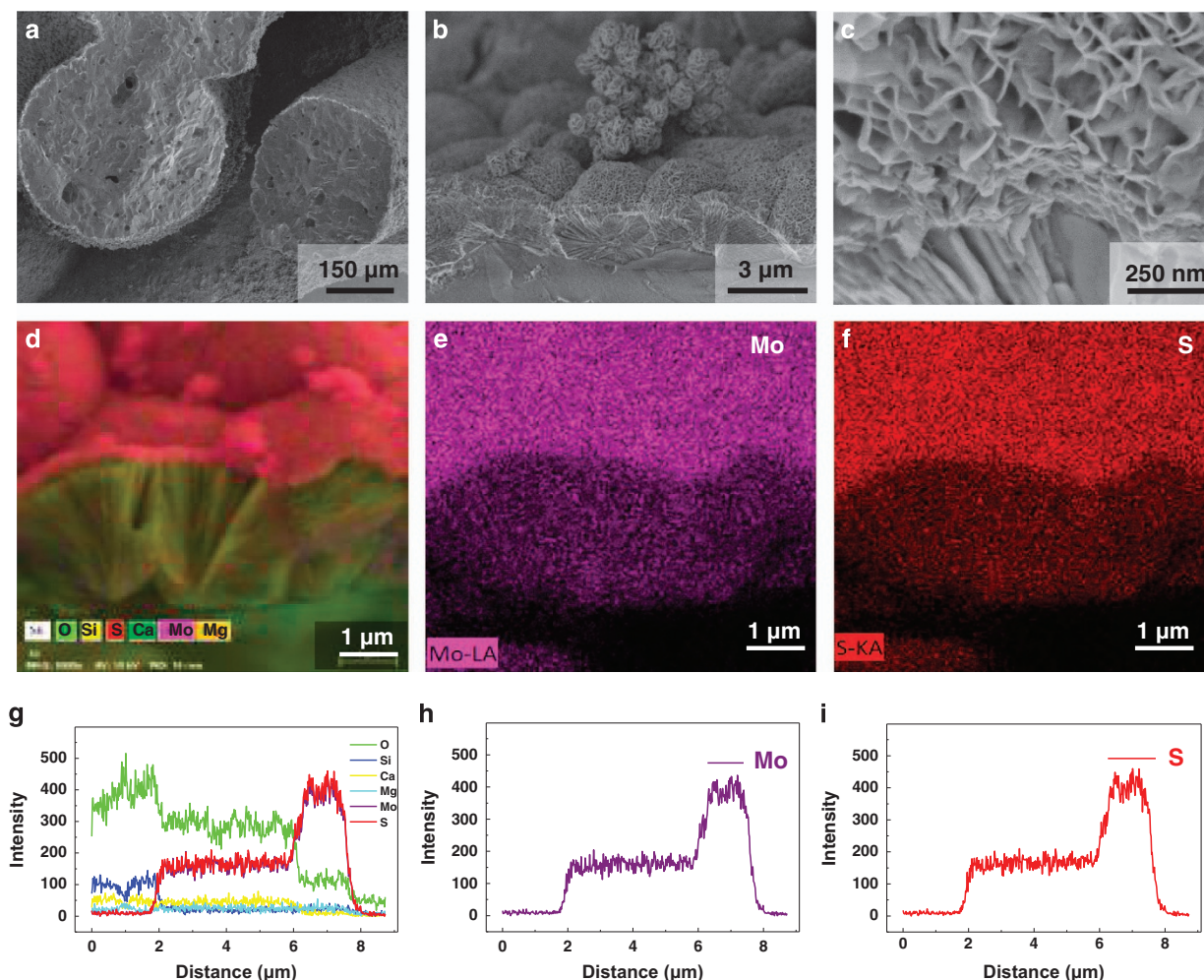
Figure 2 Fracture morphologies of 0.2 MoS₂-modified akermanite (MS-AKT) scaffolds at different magnifications (**a**–**c**). The formed core/shell structures with an akermanite (AKT) core and molybdenum disulfide (MoS₂) shell of ~5 μm thickness were clearly observed. energy-dispersive spectrometer (EDS) elemental mapping of the cross-section of MoS₂-AKT interface: all elements (**d**), element Mo (**e**), element S (**f**); EDS line scanning profiles of all elements (**g**), element Mo (**h**) and element S (**i**) from the interior to the strut surface of the scaffolds, which exhibited a step profile, confirming the elemental interpermeation between MoS₂ and AKT.

peaks at 13.7°, 32.4°, 35.1°, 50.3° and 57.9° in the XRD pattern of the MoS₂ could be indexed to the (002), (100), (102), (105) and (110) planes of the hexagonal MoS₂ phase, respectively (JCPDS card no. 37-1492).

Photothermal performance of MS-AKT scaffolds

As depicted in Figure 4, under irradiation at a power density of $0.50 \, W \, cm^{-2}$, the surface temperature of MS-AKT scaffolds rapidly increased and then reached equilibrium. The final temperature reached 115 °C within 5 min in a dry environment and 50 °C within 10 min in a wet environment. In remarkable contrast, the AKT scaffolds showed negligible temperature increases under the same irradiation condition. In addition, the photothermal temperature of MS-AKT scaffolds could be effectively modulated by altering the scaffold sizes, laser power densities or MoS₂ content (Figure 5). Specifically, as the scaffold size increased from 6 to 11 mm, the final temperature increased from 107 to 120 °C in a dry environment and from 38 to 55 °C in a wet environment (Figure 5a and b). The MS-AKT scaffold also exhibited a marked laser-dependent photo-thermal effect (Figure 5c and d): the final temperature of the MS-AKT

scaffold could be modulated in the range of 73–144 °C in a dry environment and 34–50 °C in a wet environment by altering the laser power densities in the range of 0.2–$0.6 \, W \, cm^{-2}$. The MoS₂ content did not significantly enhance the photothermal effect of MS-AKT; as shown in Figure 5e and f, the temperatures of 0.2 MS-AKT in dry and wet environments were 126 and 50 °C, respectively, slightly higher than the temperature of 0.05 MS-AKT (117 and 48 °C, respectively).

In vitro anticancer effects of MS-AKT scaffolds

Bone tumor cells (Saos-2) and breast cancer cells (MDA-MB-231) were used as models to investigate the *in vitro* anticancer effects of MS-AKT scaffolds. As shown in Figure 6a and Supplementary Figure S6, only a minority of Saos-2 cells (26%) and MDA-MB-231 cells (23%) survived the high temperature induced by MS-AKT scaffolds under NIR irradiation. For comparison, the percentages of viable cells in the MS-AKT, AKT+laser, laser and AKT groups did not significantly differ from that of the control group (Blank). In addition, more tumor cells were killed with the increase of the duration of irradiation, final temperature and irradiation times (Figure 6b–d).
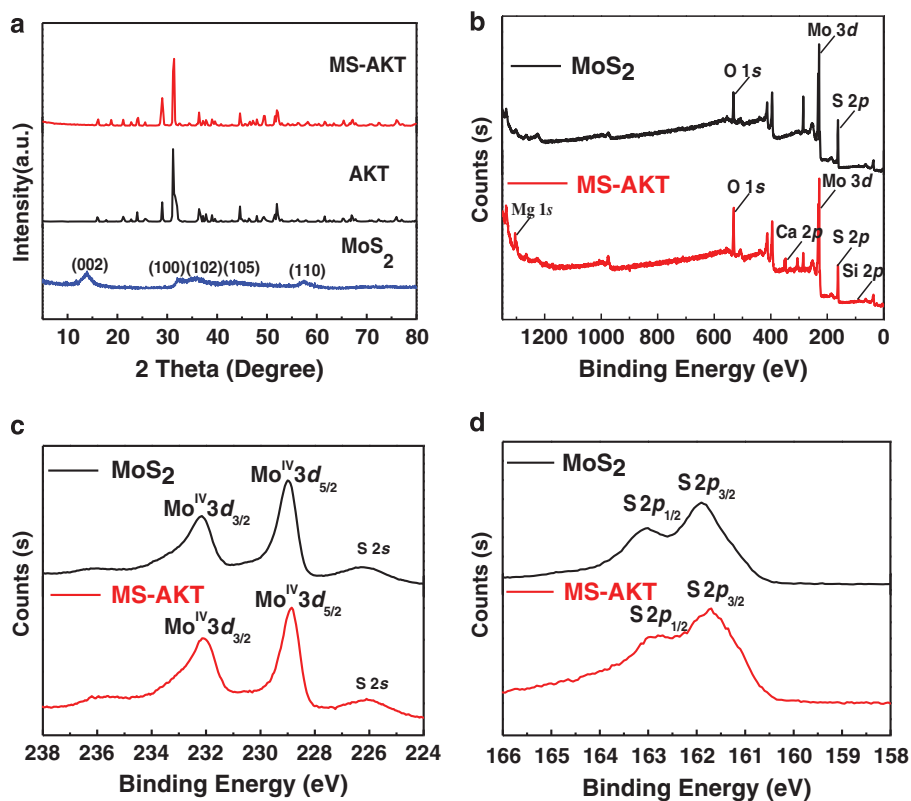
Figure 3 (**a**) X-ray diffraction (XRD) patterns of molybdenum disulfide (MoS_2) powders, Akermanite (AKT) scaffolds and MoS_2-modified akermanite (MS-AKT) scaffolds. (**b**) XPS spectrum of MoS_2 and MS-AKT scaffolds; XPS characteristic spectrum for Mo 3d (**c**) and S 2p (**d**) electrons of MoS_2 and MS-AKT scaffolds, which demonstrated valence state of +4 and −2 for Mo and S in the newly formed MoS_2 layer on the scaffolds.

Specifically, three repeated irradiation treatments by an NIR laser decreased the viability of tumor cells in the MS-AKT to nearly 5%.

SEM images showed that Saos-2 cells spread well on the surface of AKT scaffolds irrespective of laser irradiation, exhibiting dendritic pseudopodia and close attachment to the struts, and similar observations were made for MS-AKT scaffolds without laser irradiation (Figure 6f–h). In contrast, few Saos-2 cells were observed in laser-irradiated MS-AKT scaffolds, and the morphology of cells indicated cell damage (Figure 6e). Live/dead staining of Saos-2 and MDA-MB-231 cells (Figure 6m–p and Supplementary Figure S7) showed rounded, red-fluorescent cells adjacent to MS-AKT scaffolds after irradiation, indicating that cellular membrane integrity was compromised. In contrast, cells in the remaining three groups all exhibited green fluorescence, indicating live cells. After incubation for another 12 h, a large portion of Saos-2 cells (Figure 6i–l) and MDA-MB-231 cells (Supplementary Figure S8) in the MS-AKT+laser group detached, further demonstrating that hyperthermia induced by MS-AKT scaffold under NIR irradiation killed the majority of tumor cells.

In vivo tumor therapy efficacy of MS-AKT scaffolds
As shown in Figure 7b, the tumor temperature of the MS-AKT+laser group quickly increased to ~50 °C, whereas the temperature of the AKT+laser group was ~38 °C. Notably, although the temperature of the tumors exceeded 45 °C, the temperature of the surrounding healthy tissues was below 40 °C (Figure 7a). The whole-body bioluminescent signals of tumors in the MS-AKT+laser group had markedly decreased on day 7 (Figure 7c), and the tumors did not recur within 14 days (Figure 7e). After 2 weeks, the tumors of the MS-AKT, AKT and AKT+laser groups had grown ~4-fold in

volume (Figure 7d), whereas the tumors in the MS-AKT+laser group significantly shrank after NIR irradiation and had almost disappeared by day 14 (Figure 7f). The ablation efficacy of MS-AKT scaffolds was further assayed by hematoxylin and eosin staining, which showed more vacuoles, condensed nuclei, and changes in cell shape in the tumors from the MS-AKT+laser group, whereas apoptosis could not be detected in the other groups (Figure 8a–d). The quantitative analysis (Figure 8e) showed that 89% of tumor cells in the MS-AKT group were necrotic, whereas this proportion was much lower in other groups.

In vitro attachment, proliferation and osteogenic differentiation of rBMSCs
To investigate the cytocompatibility and osteogenic potential of the MS-AKT scaffold, we incubated rBMSCs (bone-forming cells) with the scaffolds, which showed that cells spread well and closely attached to the MS-AKT (Figure 9a and b and Supplementary Figure S9a and b) and AKT scaffolds (Figure 9c and d and Supplementary Figure S9c and d) throughout the entire scaffold. A CCK8 analysis (Figure 9e) showed that the proliferation of rBMSCs cultured with MS-AKT and AKT scaffolds did not significantly differ by time point (1, 3 or 7 days). The expression levels of several osteogenic differentiation markers of rBMSCs in MS-AKT and AKT scaffolds on day 7 are shown in Figure 9f–h. MS-AKT scaffolds up-regulated bone-related gene expression, including Runx2 and OCN, compared to the blank control and AKT scaffolds. The ionic concentrations of the original MS-AKT and AKT scaffold extracts (Supplementary Table S1) showed that Mo ions could be released from MS-AKT scaffolds at a concentration of 109.8 mg l^{-1} in the culture medium.
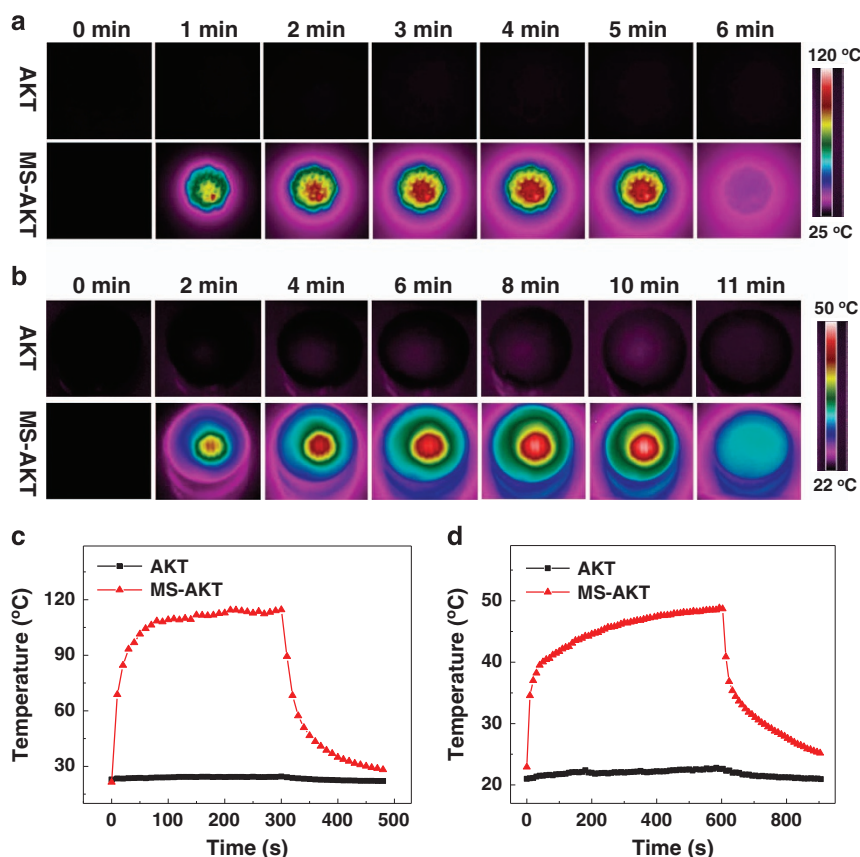
Figure 4 Real-time near-infrared (NIR) thermal images of MoS$_2$-modified akermanite (MS-AKT) and AKT scaffolds at dry (**a**) and wet (**b**) environments under continuous irradiation of 808 nm laser at the power density of 0.50 W cm^{-2}; The heating curves of MS-AKT and AKT scaffolds at dry (**c**) and wet (**d**) environment as a function of the irradiation time. The laser was shut off after 5-min irradiation at dry environments (**a**, **c**) or after 10-min irradiation at wet environment (**b**, **d**). MS-AKT scaffolds showed a strong photothermal conversion efficiency and could be rapidly and effectively heated up under 808-nm laser irradiation in comparison with AKT scaffolds.

Furthermore, the Ca and Mg concentrations in the MS-AKT extracts were similar to those in the AKT extract, indicating that inorganic ions (Mg and Ca ions) could be released from the inner ceramic core. Low concentrations ($<1/4$) of MS-AKT extract significantly stimulated the proliferation of rBMSCs compared with the AKT groups without MoS$_2$ (Supplementary Figure S10). Furthermore, lower concentrations (1/8 and 1/32) up-regulated the expression of osteogenic genes (Runx2, OCN, OPN and ALP) by rBMSCs in MS-AKT scaffold extracts on day 7 compared to the AKT extracts and blank control groups (Supplementary Figure S11).

In vivo bone regeneration under short-term photothermal treatment

The temperature in the bone defect sites of rabbits implanted with MS-AKT scaffolds reached $\sim 50\,^\circ$C, whereas the temperature of the AKT group only increased to 38 °C under NIR irradiation (Figure 10j and Supplementary Figure S14b). As demonstrated by micro-CT, both MS-AKT and AKT scaffolds implanted in the femoral defects of rabbits induced new bone formation in the macropores and the surrounding area of the scaffolds 8 weeks after implantation (Figure 10a–d), and the relative bone volume fraction (BV/TV) did not significantly differ between the two groups (Figure 10i). The Van Gieson's picrofuchsin staining images further confirmed that both scaffolds induced the formation of new bone in the scaffolds (Figure 10e–h).

DISCUSSION

Considering the high photothermal performance of MoS$_2$ and the physiological function of Mo, two-dimensional MoS$_2$ was employed to fabricate a novel 3D-printed bifunctional bioceramic scaffold in our study. MoS$_2$-modified scaffolds were successfully prepared by combining a 3D printing technique with a hydrothermal method. Owing to the MoS$_2$ nanosheets grown on the strut surface, the MS-AKT scaffold showed excellent photothermal performance and thereby effectively ablated tumor cells *in vitro* and *in vivo*. Moreover, the excellent osteogenic potential of AKT scaffolds was maintained, and the novel scaffolds induced new bone ingrowth in the critical-sized femoral defects of rabbits without being affected by short-term NIR irradiation. Thus, the prepared MS-AKT scaffolds both provide tumor therapy and stimulate bone regeneration to treat tumor-related bone defects (Scheme 1b).

In this study, we, for the first time, fabricated bifunctional scaffolds via the *in situ* growth of MoS$_2$ nanosheets on the strut surface of 3D-printed AKT bioceramic scaffolds by combining a 3D printing technique with a hydrothermal method. The MoS$_2$ layer integrated well with the substrate of AKT bioceramics and remained stable even after ultrasonication. The growth of MoS$_2$ nanosheets on 3D-printed bioceramic scaffolds can be summarized as follows. First, AKT bioceramic scaffolds with highly interconnected and well-ordered pore structures were prepared by 3D printing. The AKT scaffolds were immersed in an aqueous precursor solution containing (NH$_4$)$_6$
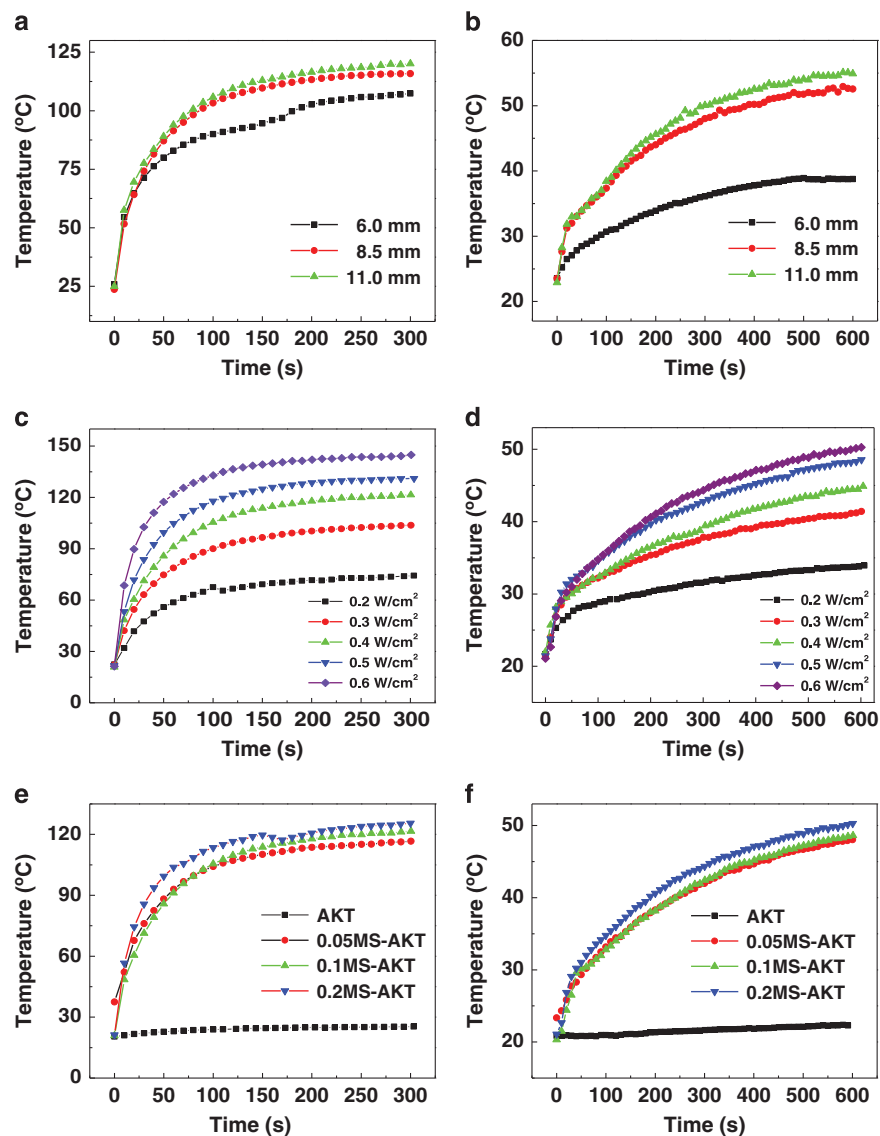
Figure 5 Photothermal heating curves of MoS$_2$-modified akermanite (MS-AKT) scaffolds with different sizes (diameter: 6.0 mm, 8.5 mm, 11.0 mm) at dry (**a**) and wet (**b**) environment under 808-nm laser irradiation at the power density of 0.50 W cm^{-2}; Photothermal heating curves of MS-AKT scaffolds (diameter: 8.5 mm) at different laser power density (0.2, 0.3, 0.4, 0.5 and 0.6 W cm^{-2}) at dry (**c**) and wet (**d**) environment; Photothermal heating curves of MS-AKT scaffolds with different contents of MoS$_2$ at dry (**e**) and wet (**f**) environment (808 nm, 0.5 W cm^{-2}). The final temperature of MS-AKT scaffolds could be well modulated by altering the scaffold sizes, laser power densities and MoS$_2$ contents.

Mo$_7$O$_{24}$·4H$_2$O and H$_2$NCSNH$_2$. H$_2$NCSNH$_2$ then adsorbed to the surface of AKT via amidogen.[35] Under hydrothermal conditions, H$_2$NCSNH$_2$ decomposed and anchored to the strut surface of the AKT scaffolds. Next, the nucleation and growth of the sheet-like MoS$_2$ proceeded *in situ*, with AKT scaffolds serving as templates. Finally, MS-AKT composite scaffolds were successfully generated with MoS$_2$ nanosheets assembled on the surface of AKT. The morphologies and chemical status of the MoS$_2$ layer on the scaffold surface were similar to those of pure MoS$_2$ particles prepared by the same hydrothermal route,[33] indicating that the hydrothermal synthesis of MoS$_2$ was not interrupted by the presence of AKT scaffolds. Moreover, a general core/shell structure formed that consisted of three regions from the strut surface to the interior of MS-AKT scaffolds: (1) a spongy MoS$_2$ shell rich in Mo and S; (2) a relatively loose transition region consisting of Mo, S, Ca, Mg, Si and O; and (3) a dense AKT core rich in Ca, Mg, Si and O. Thus, Mo and S in the precursor

solution likely permeated into the AKT interior during the hydro-thermal process and some Ca, Mg, Si and O from the AKT scaffolds simultaneously diffused into the newly synthesized MoS$_2$ layer to form a continuous and stable bond at the MoS$_2$-AKT interface. The gradient structure confirmed the elemental interpermeation between MoS$_2$ and AKT during the hydrothermal process, indicating that MoS$_2$ nanosheets were closely bonded to the AKT ceramics. This close bonding may be primarily responsible for the unchanged the morphologies of MS-AKT scaffolds after ultrasonication. To our knowledge, this study is the first to demonstrate the growth of MoS$_2$ nanosheets on bioceramic scaffolds, and offer a more stable and controllable method to modify 3D-printed scaffolds than the direct solution-soaking method.[3] The prepared MS-AKT scaffolds could combine the photothermal effect of MoS$_2$ nanosheets for tumor therapy and porous structure for bone regeneration, avoiding the shortcomings of simple MoS$_2$ particles or AKT scaffolds.
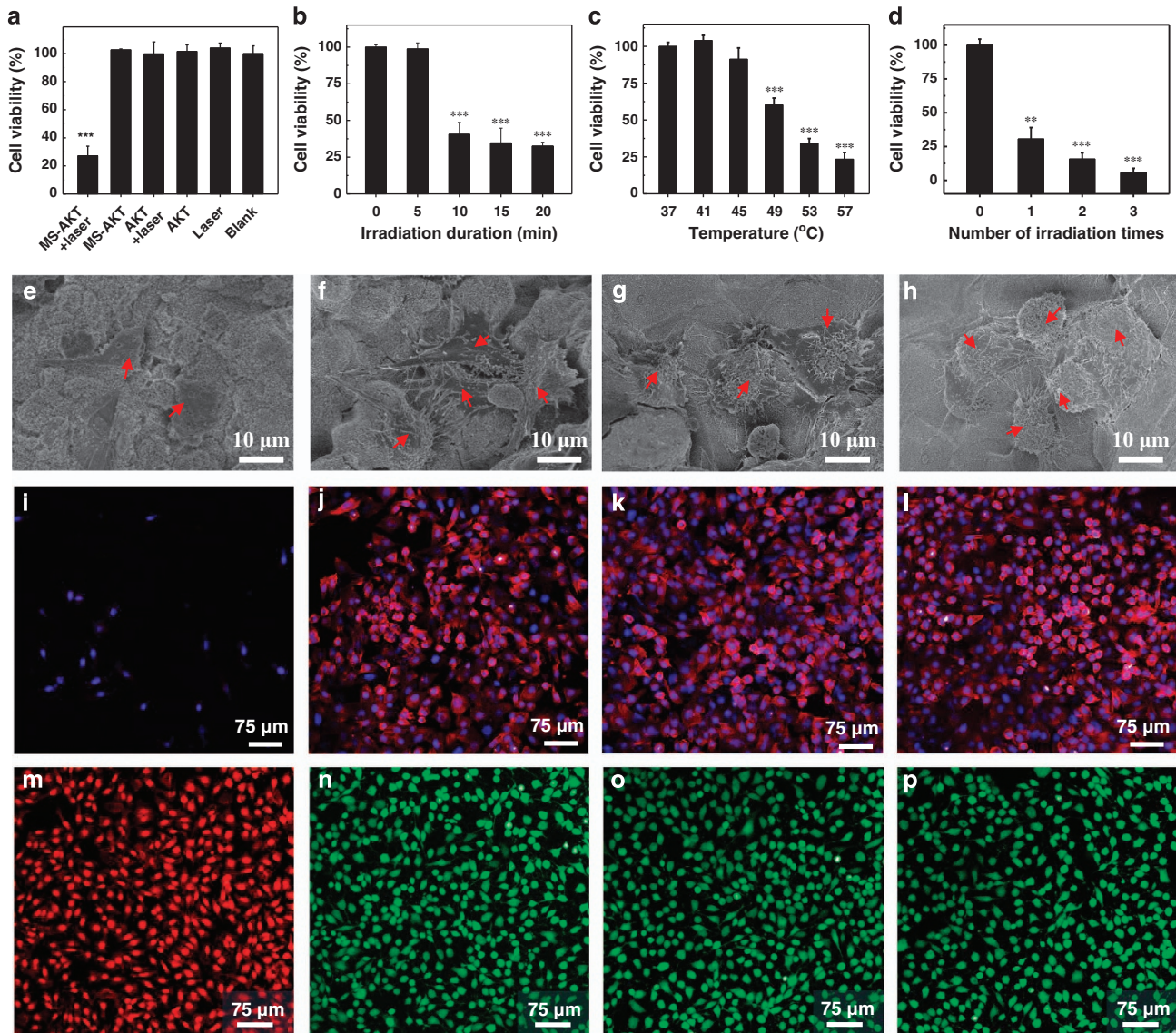
Figure 6 Relative cell viability of bone tumor cells (Sao-2) treating with different conditions: (**a**) akermanite (AKT) and MoS$_2$-modified AKT (MS-AKT) scaffolds with or without NIR treatment (808 nm, 0.6 W cm^{-2}, 10 min); (**b**) MS-AKT scaffolds with different irradiation duration (808 nm, 0.6 W cm^{-2}); (**c**) MS-AKT scaffolds under different temperature (808 nm, 10 min); (**d**) MS-AKT scaffolds with different irradiation times (808 nm, 0.6 W cm^{-2}, 10 min). (*$P<0.05$, **$P<0.01$, ***$P<0.001$). SEM (**e–h**, cells shown by red arrows), confocal LSM (**i–l**; red: cytoskeleton; blue: cell nuclei) and live/dead staining (m-p; green: live cells; red: dead cells) images of Saos-2 cells in MS-AKT scaffolds with laser irradiation (**e, i** and **m**) and without laser irradiation (**f, j** and **n**), AKT scaffolds with laser irradiation (**g, k** and **o**) and without laser irradiation (**h, l** and **p**). MS-AKT scaffolds effectively killed tumor cells, showing excellent *in vitro* anticancer effect under NIR irradiation.

Because of their intense localized surface plasmon resonances, single- or few-layer MoS$_2$ nanosheets displayed an absorbance profile reaching the NIR region, where biological systems are maximally transparent.[12,13] This intrinsic physical property contributes to the excellent photothermal conversion efficacy of MoS$_2$ nanosheets under 808-nm laser irradiation. In our study, the newly synthesized MoS$_2$ nanosheets were efficiently grown on the strut surfaces of AKT scaffolds, endowing the scaffolds with excellent 'inherent' photothermal-transducing ability. With the assistance of MoS$_2$ nanosheets, MS-AKT scaffolds could be rapidly and effectively heated under 808-nm laser irradiation. More importantly, the temperature of MS-AKT scaffolds was easily modulated in a wide range, from room temperature to 144 °C, by controlling the MoS$_2$ content, scaffold size and power density of the NIR laser. This attractive photothermal

feature of MS-AKT scaffolds is expected to greatly favor the further *in vitro* and *in vivo* photothermal ablation of tumor cells in a controllable manner.

We then evaluated the photothermal therapeutic efficiency of MS-AKT scaffolds by ablating tumor cells *in vitro* and *in vivo*. Our results indicate that the high and controllable temperature induced by the photothermal effect of MS-AKT scaffolds was able to reduce the viability of tumor cells to nearly 5% *in vitro*. Specifically, a 5 °C increase in temperature has been reported as the minimum temperature required for cancer hyperthermia therapy.[36] Slightly lower temperatures (> 40 °C) temporarily inactivate cells for several hours, 'severe' hyperthermia treatments (43–45 °C) result in long-term cell inactivation, 'suppressive hyperthermia' (45–48 °C) produces rapid necrotic cell death, and temperatures above 48 °C result in drastic cell
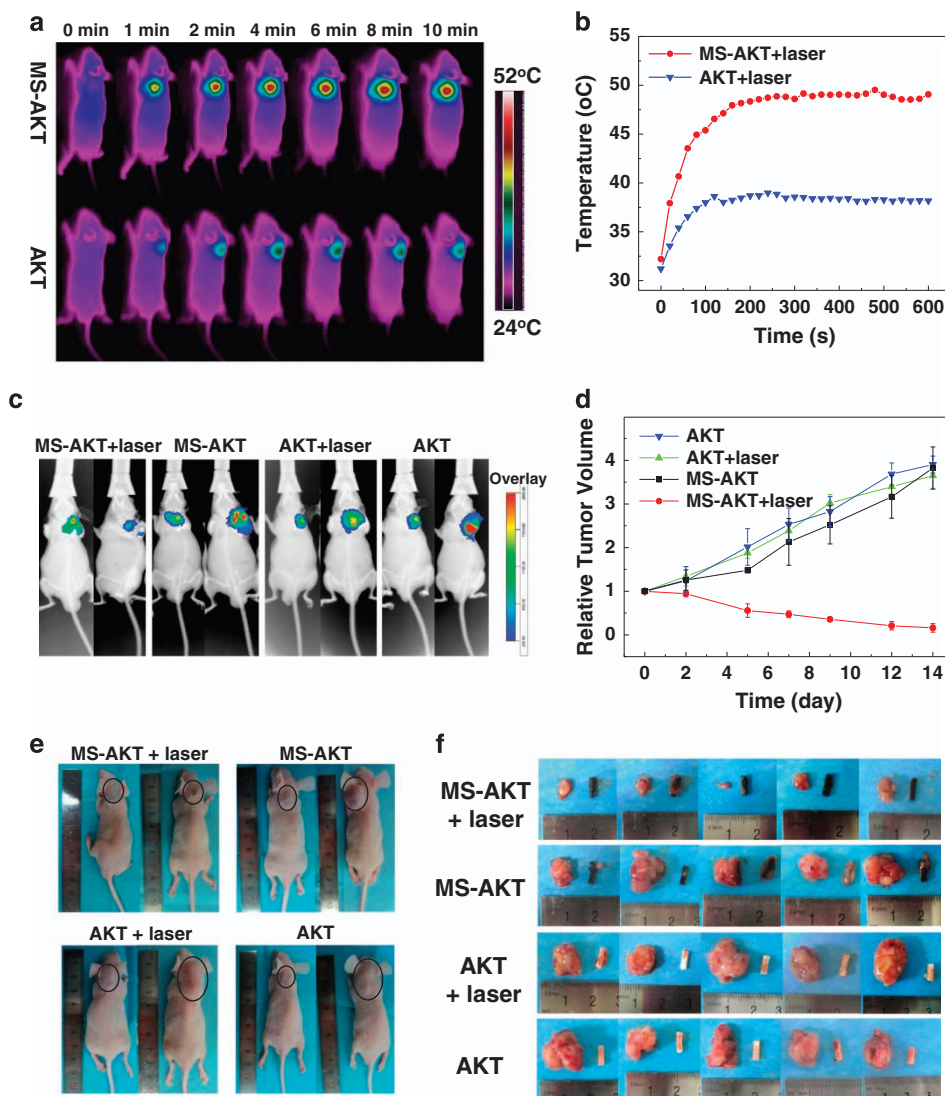
Figure 7 Near-infrared (NIR) thermal images (**a**) and heating curves (**b**) of tumor-bearing mice post-implanted with MoS$_2$-modified akermanite (MS-AKT) and AKT scaffolds under the 808-nm laser irradiation taken at different time intervals; The whole-body fluorescence imaging (**c**) of tumor after various different treatments at day 0 (left) and day 7 (right), and representative photograph (**e**) of mice after various different treatments indicated at day 0 (left) and day 14 (right); (**d**) Relative tumor volume in four groups with increasing days ($n=5$); (**f**) Photograph of tumors obtained from four groups at day 14. Hyperthermia induced by photothermal effect of MS-AKT scaffolds efficiently inhibited tumor growth *in vivo*.

death.[37] In this study, the temperatures of tumors implanted with MS-AKT scaffolds increased rapidly up to 45 °C within 60 s and could readily reach ~ 50 °C, which most likely resulted in apoptosis and tumor ablation. In contrast, the temperature of tumors implanted with AKT scaffolds did not significantly change under the same irradiation conditions. Therefore, MS-AKT scaffolds with desirable photothermal performance may be a promising biomaterial for inhibiting tumor growth.

In addition to their anticancer capacity, the osteogenic potential of implanted scaffolds for treating tumor-induced bone defects is equally important. Our previous studies have demonstrated that soluble Ca, Si and Mg ions released from AKT (Ca$_2$MgSi$_2$O$_7$) bioceramics up-regulated the expression of osteogenesis- and angiogenesis-related genes.[38,39] Compared with β-TCP (Ca$_3$PO$_4$, representative of bioceramics), AKT not only promoted cell attachment, proliferation, osteogenic differentiation and angiogenesis *in vitro* but also enhanced *in vivo* osteogenesis and angiogenesis.[31,32,40] Therefore, AKT was

employed as the model material for growing MoS$_2$ nanosheets to fabricate MS-AKT scaffolds, and the osteogenic potential of these scaffolds was evaluated in the present study. The *in vitro* experiments demonstrated that both MS-AKT and AKT scaffolds supported the attachment and proliferation of rBMSCs, and even low concentrations of MS-AKT extracts significantly enhanced the proliferation of rBMSCs compared to AKT groups without MoS$_2$. In addition, we found that MS-AKT scaffolds and their extracts enhanced the expression of bone-related genes, such as OPN, OCN, Runx2 and ALP. MS-AKT scaffolds likely promote *in vitro* osteogenesis via Mo ions released from these scaffolds. Thus, we further examined the osteogenic potential MS-AKT and AKT scaffolds *in vivo* by implanting them into critical-sized femoral defects in rabbits for 8 weeks. To explore the effect of short-term PTT on long-term bone regeneration, both scaffolds were irradiated with an 808-nm laser, similar to the scaffolds implanted in tumor-bearing mice. Both MS-AKT and AKT scaffolds induced new bone formation in the
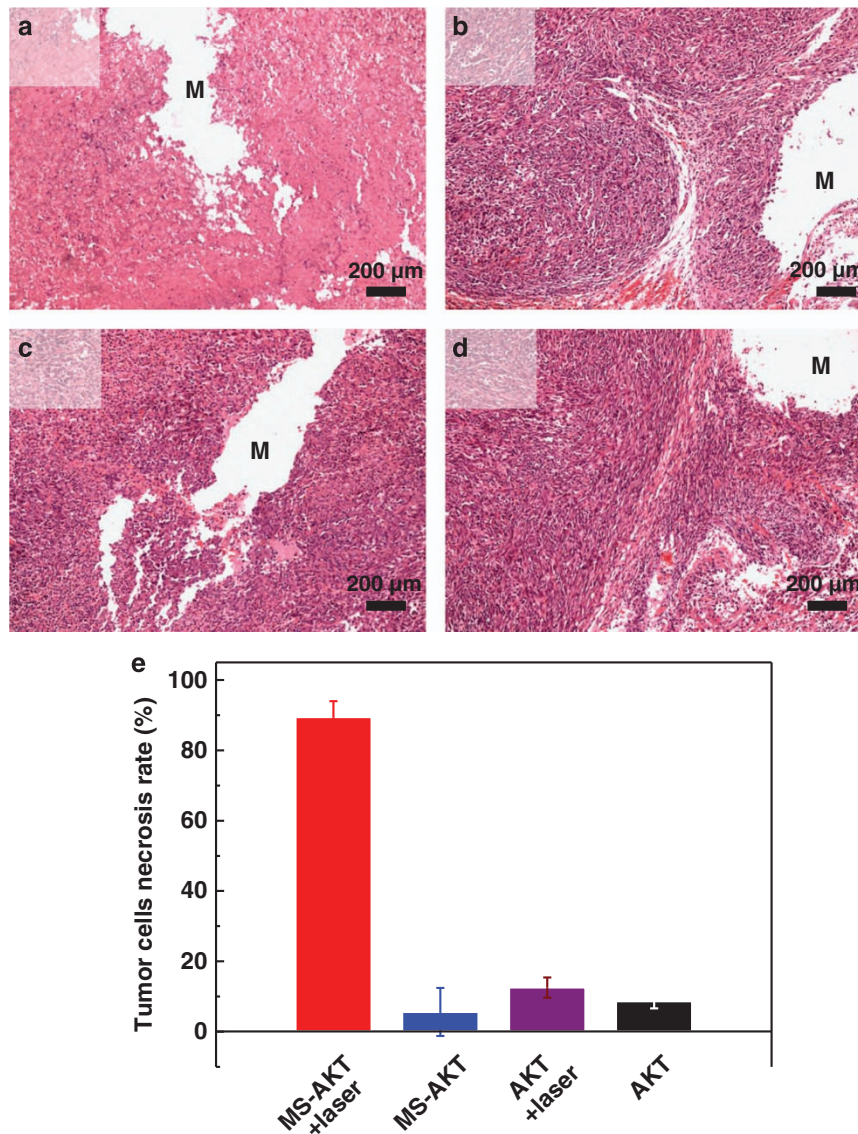
Figure 8 Hematoxylin and eosin (H&E) staining images of osteosarcoma (Saos-2) tumor tissue implanted with MoS₂-modified akermanite (MS-AKT) scaffolds with (**a**) and without near-infrared (NIR) irradiation (**b**), AKT scaffolds with (**c**) and without (**d**) NIR irradiation. M represents implanted scaffold material. (**e**) The tumor cells necrosis rate of four groups. Hyperthermia induced by photothermal effect of MS-AKT scaffolds distinctly induced the apoptosis of tumor cells *in vivo*.

macropores and area surrounding the scaffolds, and this growth did not significantly differ between the two groups, indicating that the *in situ* growth of MoS₂ nanosheets on AKT scaffolds did not negatively affect the formation of new bone and that long-term bone regeneration was not affected by short-term NIR irradiation. These preliminary results suggested that MS-AKT scaffolds exhibited excellent osteogenic potential *in vivo* and may serve as bioactive materials for repairing large bone defects.

In our work, the bifunctionality of MS-AKT scaffolds, that is, their photothermal therapeutic and osteogenic potentials, were separately demonstrated both *in vitro* and *in vivo*. Whereas establishing critical-sized bone defects in mice is unconvincing due to their small bones compared to the large size of the scaffolds, bone cancer models in rabbits or larger animals are not available because tumors are difficult to establish in these animals due to immunological rejection. Therefore, the photothermal effect of scaffolds for tumor therapy

was investigated in rabbit models. Overall, the obtained bifunctional scaffolds exhibit the following advantages. First, a controllable hydrothermal process enables *in situ* MoS₂ nanosheet growth on the strut surfaces of AKT scaffolds, endowing the scaffolds with stable nanostructures. Second, MS-AKT scaffolds could be precisely implanted into the tumors, where they provided effective localized PTT. Third, the photothermal effect could be controlled to ablate the tumor, which mitigated side effects on surrounding normal tissues. Our results showed that the controllable NIR laser irradiation and the excellent photothermal effect of MS-AKT scaffolds resulted in a center temperature of the tumors that exceeded 50 °C, whereas the temperature of the surrounding healthy tissues was below 40 °C, suggesting MS-AKT scaffolds could efficiently kill the tumor cells under irradiation without damaging the surrounding healthy tissues. Finally, the scaffolds maintained good biocompatibility and exhibited excellent osteogenic potential *in vivo*, even upon
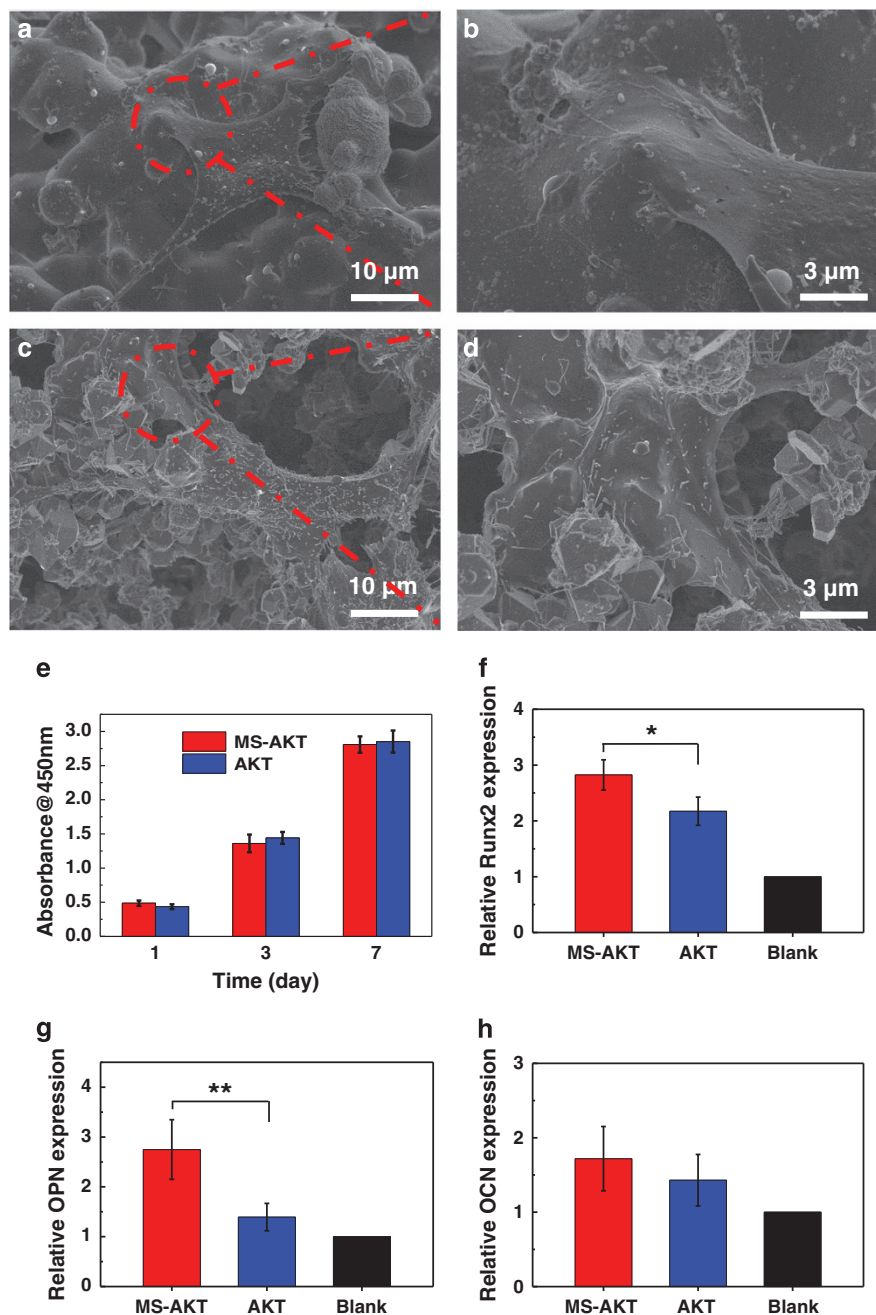
Figure 9 SEM images of rBMSCs on the strut surface of MoS$_2$-modified akermanite (MS-AKT) (**a**, **b**) and AKT (**c**, **d**) scaffolds after incubation for 3 days. The cell proliferation (**e**) and osteogenic gene expression (Runx2, OPN and OCN) (**f–h**) of rBMSCs in the MS-AKT and AKT scaffolds at day 7. (*$P < 0.05$, **$P < 0.01$). Cells spread well and closely attached on both MS-AKT and AKT scaffolds. The proliferation of rabbit bone mesenchymal stem cells (rBMSCs) cultured with MS-AKT and AKT scaffolds had no significant difference at each time point (1, 3 and 7 days), indicating the good cytocompatibility of MS-AKT scaffolds. MS-AKT scaffolds could stimulate bone-related gene expression of rBMSCs, including Runx2 and OPN.

exposure to NIR irradiation. Thus, our study opens a new and interesting avenue in the development of two-dimensional transitional metal dichalcogenide for tissue engineering and tumor therapy applications.

CONCLUSION

In summary, a bifunctional scaffold was successfully prepared by growing MoS$_2$ nanosheets on 3D-printed bioceramic scaffolds *in situ* via a facile hydrothermal process. The newly formed MoS$_2$ layer endowed the scaffolds with controllable photothermal effects. Specifically, the high temperature significantly decreased tumor cell viability *in vitro* and inhibited tumor growth *in vivo*. Moreover, the MS-AKT scaffolds supported the attachment, proliferation and osteogenic differentiation of rBMSCs and induced bone regeneration *in vivo*. Therefore, such a bifunctional scaffold, which both provides tumor therapy and promotes bone growth, offers a promising clinical strategy for the effective treatment of tumor-induced bone defects.
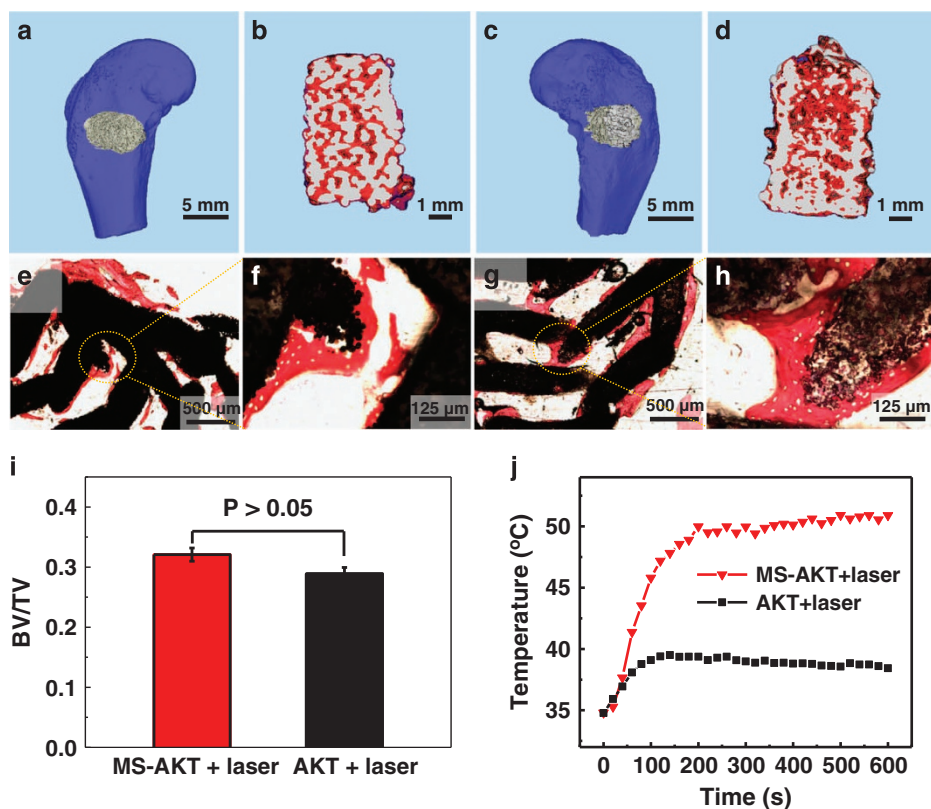
Figure 10 Micro-CT analysis for the bone regeneration after implanting with MoS$_2$-modified akermanite (MS-AKT) (**a**, **b**) and AKT (**c**, **d**) scaffolds in the critical-sized femoral defects of rabbits for 8 weeks. Red color stands for the formation of new bone (**b**, **d**). Histological analysis of MS-AKT (**e**, **f**) and AKT (**g**, **h**) scaffolds by Van Gieson staining after implanting for 8 weeks. (**i**) Quantitative analysis for new bone formation by Micro-CT analysis. (**j**) The heating curves of rabbits under near-infrared (NIR) irradiation (0.5 W cm^{-2}, 10 min) to explore short-time photothermal treatment on long-term bone regeneration. Both MS-AKT and AKT scaffolds induced new bone formation around the scaffolds and in the macropores. There was no significant difference between two groups, indicating that *in situ* growth of MoS$_2$ on AKT scaffolds had no obvious negative effect on formation of new bone and long-term bone regeneration was not affected by short-time NIR irradiation. MS-AKT scaffolds displayed excellent bone-forming ability *in vivo*.

CONFLICT OF INTEREST

The authors declare no conflict of interest.

1 Verron, E., Schmid-Antomarchi, H., Pascal-Mousselard, H., Schmid-Alliana, A., Scimeca, J.-C. & Bouler, J.-M. Therapeutic strategies for treating osteolytic bone metastases. *Drug Discov. Today* **19**, 1419–1426 (2014).

2 Cheng, L., Wang, C., Feng, L., Yang, K. & Liu, Z. Functional nanomaterials for phototherapies of cancer. *Chem. Rev.* **114**, 10869–10939 (2014).

3 Ma, H., Jiang, C., Zhai, D., Luo, Y., Chen, Y., Lv, F., Yi, Z., Deng, Y., Wang, J. & Chang, J. A bifunctional biomaterial with photothermal effect for tumor therapy and bone regeneration. *Adv. Funct. Mater.* **26**, 1197–1208 (2016).

4 Marques, C., Ferreira, J., Andronescu, E., Ficai, D., Sonmez, M. & Ficai, A. Multifunctional materials for bone cancer treatment. *Int. J. Nanomed.* **9**, 2713–2725 (2014).

5 Peer, D., Karp, J. M., Hong, S., Farokhzad, O. C., Margalit, R. & Langer, R. Nanocarriers as an emerging platform for cancer therapy. *Nat. Nanotechnol.* **2**, 751–760 (2007).

6 Hainfeld, J. F., Dilmanian, F. A., Slatkin, D. N. & Smilowitz, H. M. Radiotherapy enhancement with gold nanoparticles. *J. Pharm. Pharmacol.* **60**, 977–985 (2008).

7 Cheng, L., He, W., Gong, H., Wang, C., Chen, Q., Cheng, Z. & Liu, Z. PEGylated micelle nanoparticles encapsulating a non-fluorescent near-infrared organic dye as a safe and highly-effective photothermal agent for *in vivo* cancer therapy. *Adv. Funct. Mater.* **23**, 5893–5902 (2013).

8 Liu, H., Chen, D., Li, L., Liu, T., Tan, L., Wu, X. & Tang, F. Multifunctional gold nanoshells on silica nanorattles: a platform for the combination of photothermal therapy and chemotherapy with low systemic toxicity. *Angew. Chem. Int. Ed.* **123**, 921–925 (2011).

9 Robinson, J. T., Tabakman, S. M., Liang, Y., Wang, H., Sanchez Casalongue, H., Vinh, D. & Dai, H. Ultrasmall reduced graphene oxide with high near-infrared absorbance for photothermal therapy. *J. Am. Chem. Soc.* **133**, 6825–6831 (2011).

10 Qu, Y., Chu, B., Peng, J. R., Liao, J. F., Qi, T. T., Shi, K., Zhang, X. N., Wei, Y. Q. & Qian, Z. Y. A biodegradable thermo-responsive hybrid hydrogel: therapeutic applications in preventing the post-operative recurrence of breast cancer. *NPG Asia Mater.* **7**, 10 (2015).

11 Yong, Y., Zhou, L. J., Zhang, S. S., Yan, L., Gu, Z. J., Zhang, G. J. & Zhao, Y. L. Gadolinium polytungstate nanoclusters: a new theranostic with ultrasmall size and versatile properties for dual-modal MR/CT imaging and photothermal therapy/radiotherapy of cancer. *NPG Asia Mater.* **8**, 11 (2016).

12 Zhang, X., Lai, Z., Tan, C. & Zhang, H. Solution-processed two-dimensional MoS$_2$ nanosheets: preparation, hybridization, and applications. *Angew. Chem. Int. Ed.* **55**, 8816–8838 (2016).

13 Chou, S. S., Kaehr, B., Kim, J., Foley, B. M., De, M., Hopkins, P. E., Huang, J., Brinker, C. J. & Dravid, V. P. Chemically exfoliated MoS$_2$ as near-infrared photothermal agents. *Angew. Chem. Int. Ed.* **125**, 4254–4258 (2013).

14 Eda, G., Yamaguchi, H., Voiry, D., Fujita, T., Chen, M. & Chhowalla, M. Photoluminescence from chemically exfoliated MoS$_2$. *Nano Lett.* **11**, 5111–5116 (2011).

15 Wang, S. G., Li, K., Chen, Y., Chen, H. R., Ma, M., Feng, J. W., Zhao, Q. H. & Shi, J. L. Biocompatible PEGylated MoS$_2$ nanosheets: controllable bottom-up synthesis and highly efficient photothermal regression of tumor. *Biomaterials* **39**, 206–217 (2015).

16 Liu, T., Shi, S., Liang, C., Shen, S., Cheng, L., Wang, C., Song, X., Goel, S., Barnhart, T. E. & Cai, W. Iron oxide decorated MoS$_2$ nanosheets with double PEGylation for chelator-free radiolabeling and multimodal imaging guided photothermal therapy. *ACS Nano* **9**, 950–960 (2015).

17 Yin, W., Yan, L., Yu, J., Tian, G., Zhou, L., Zheng, X., Zhang, X., Yong, Y., Li, J. & Gu, Z. High-throughput synthesis of single-layer MoS₂ nanosheets as a near-infrared photothermal-triggered drug delivery for effective cancer therapy. *ACS Nano* **8**, 6922–6933 (2014).

18 Liu, T., Wang, C., Gu, X., Gong, H., Cheng, L., Shi, X., Feng, L., Sun, B. & Liu, Z. Drug delivery with PEGylated MoS₂ nano-sheets for combined photothermal and chemotherapy of cancer. *Adv. Mater.* **26**, 3433–3440 (2014).

19 Xu, M., Li, H., Zhai, D., Chang, J., Chen, S. & Wu, C. Hierarchically porous nagelschmidtite bioceramic-silk scaffolds for bone tissue engineering. *J. Mater. Chem. B* **3**, 3799–3809 (2015).

20 Do, A. V., Khorsand, B., Geary, S. M. & Salem, A. K. 3D printing of scaffolds for tissue regeneration applications. *Adv. Healthc. Mater.* **4**, 1742–1762 (2015).

21 Butscher, A., Bohner, M., Hofmann, S., Gauckler, L. & Muller, R. Structural and material approaches to bone tissue engineering in powder-based three-dimensional printing. *Acta Biomater.* **7**, 907–920 (2011).

22 Hollister, S. J. Porous scaffold design for tissue engineering. *Nat. Mater.* **4**, 518–524 (2005).

23 Schwarz, G., Belaidi, A. A. in *Metal Ions in Life Sciences* Vol. 13 (eds Sigel Astrid, Sigel Helmut & Sigel Roland K. O.) Ch. 13, 415–450 (Springer Netherlands: Dordrecht, The Netherlands, 2013).

24 Dermience, M., Lognay, G., Mathieu, F. & Goyens, P. Effects of thirty elements on bone metabolism. *J. Trace Elem. Med. Biol.* **32**, 86–106 (2015).

25 Reid, B., Kurnick, A., Svacha, R. & Couch, J. The effect of molybdenum on chick and poult growth. *Exp. Biol. Med.* **93**, 245–248 (1956).

26 Howell, J. M., Shunxiang, Y. & Gawthorne, J. Effect of thiomolybdate and ammonium molybdate in pregnant guinea pigs and their offspring. *Res. Vet. Sci.* **55**, 224–230 (1993).

27 Lin, D.-J., Chuang, C.-C., Lin, J.-H. C., Lee, J.-W., Ju, C.-P. & Yin, H.-S. Bone formation at the surface of low modulus Ti–7.5 Mo implants in rabbit femur. *Biomaterials* **28**, 2582–2589 (2007).

28 Lee, J. W., Lin, D. J., Ju, C. P., Yin, H. S., Chuang, C. C. & Lin, J. H. C. *In-vitro* and *in-vivo* evaluation of a new Ti-15Mo-1Bi alloy. *J. Biomed. Mater. Res. B Appl. Biomater.* **91B**, 643–650 (2009).

29 Hedberg, Y. S., Qian, B., Shen, Z., Virtanen, S. & Odnevall Wallinder, I. *In vitro* biocompatibility of CoCrMo dental alloys fabricated by selective laser melting. *Dent. Mater.* **30**, 525–534 (2014).

30 Trentani, L., Pelillo, F., Pavesi, F., Ceciliani, L., Cetta, G. & Forlino, A. Evaluation of the TiMo₁₂Zr₆Fe₂ alloy for orthopaedic implants: *in vitro* biocompatibility study by using primary human fibroblasts and osteoblasts. *Biomaterials* **23**, 2863–2869 (2002).

31 Huang, Y., Jin, X., Zhang, X., Sun, H., Tu, J., Tang, T., Chang, J. & Dai, K. *In vitro* and *in vivo* evaluation of akermanite bioceramics for bone regeneration. *Biomaterials* **30**, 5041–5048 (2009).

32 Liu, Q., Cen, L., Yin, S., Chen, L., Liu, G., Chang, J. & Cui, L. A comparative study of proliferation and osteogenic differentiation of adipose-derived stem cells on akermanite and β-TCP ceramics. *Biomaterials* **29**, 4792–4799 (2008).

33 Xie, J. F., Zhang, J. J., Li, S., Grote, F., Zhang, X. D., Zhang, H., Wang, R. X., Lei, Y., Pan, B. C. & Xie, Y. Controllable disorder engineering in oxygen-incorporated MoS₂ ultrathin nanosheets for efficient hydrogen evolution. *J. Am. Chem. Soc.* **135**, 17881–17888 (2013).

34 Lin, K. L., Xia, L. G., Li, H. Y., Jiang, X. Q., Pan, H. B., Xu, Y. J., Lu, W. W., Zhang, Z. Y. & Chang, J. Enhanced osteoporotic bone regeneration by strontium-substituted calcium silicate bioactive ceramics. *Biomaterials* **34**, 10028–10042 (2013).

35 Peng, K., Fu, L. J., Ouyang, J. & Yang, H. M. Emerging parallel dual 2D composites: natural clay mineral hybridizing MoS₂ and interfacial structure. *Adv. Funct. Mater.* **26**, 2666–2675 (2016).

36 Huang, X., Jain, P. K., El-Sayed, I. H. & El-Sayed, M. A. Determination of the minimum temperature required for selective photothermal destruction of cancer cells with the use of immunotargeted gold nanoparticles. *Photochem. Photobiol.* **82**, 412–417 (2006).

37 Jaque, D., Maestro, L. M., Del Rosal, B., Haro-Gonzalez, P., Benayas, A., Plaza, J., Rodriguez, E. M. & Sole, J. G. Nanoparticles for photothermal therapies. *Nanoscale* **6**, 9494–9530 (2014).

38 Zhai, W., Lu, H., Wu, C., Chen, L., Lin, X., Naoki, K., Chen, G. & Chang, J. Stimulatory effects of the ionic products from Ca-Mg-Si bioceramics on both osteogenesis and angiogenesis *in vitro*. *Acta Biomater.* **9**, 8004–8014 (2013).

39 Gu, H., Guo, F., Zhou, X., Gong, L., Zhang, Y., Zhai, W., Chen, L., Cen, L., Yin, S. & Chang, J. The stimulation of osteogenic differentiation of human adipose-derived stem cells by ionic products from akermanite dissolution via activation of the ERK pathway. *Biomaterials* **32**, 7023–7033 (2011).

40 Sun, H., Wu, C., Dai, K., Chang, J. & Tang, T. Proliferation and osteoblastic differentiation of human bone marrow-derived stromal cells on akermanite-bioactive ceramics. *Biomaterials* **27**, 5651–5657 (2006).

Supplementary Information accompanies the paper on the NPG Asia Materials website (http://www.nature.com/am)